Challenges of diagnosing glaucoma in myopic eyes

Qiu, Kunliang

Chapter 2

Influence of the retinal blood vessel topography on the variability of the retinal nerve fiber bundle trajectories in the human retina

Kunliang Qiu, Julia Schiefer, Jukka Nevalainen, Ulrich Schiefer, Nomdo M. Jansonius

Invest. Ophthalmol. Vis. Sci. 2015; 56(11):6320-6325.

ABSTRACT

Purpose: To determine the relationship between the retinal blood vessel topography and the retinal nerve fiber bundle (RNFB) trajectories in the human retina.

Methods: A previously collected dataset comprising 28 fundus photographs with traced RNFB trajectories was used. For all traced trajectories, the departure from our previously published RNFB trajectory model was calculated. Subsequently, we calculated, per subject, a 'mean departure' for the superior-temporal and inferior-temporal region. We measured angles between a line connecting the optic nerve head (ONH) center and the fovea and lines connecting the ONH center and the crossings of the superior and inferior temporal arteries (arterial angles) and veins (venous angles) with circles around the ONH; circle radii were 25%, 50%, and 100% of the ONH center to fovea distance. We also defined two angles based on the location of the first arteriovenous crossing. Multiple linear regression analysis was performed with mean departure as dependent variable and refraction, ONH inclination, and vessel angles as independent variables.

Results: In the superior-temporal region, refraction (P=0.017), ONH inclination (P=0.021), and the arterial angle corresponding to the middle circle (P<0.001) were significant determinants of mean departure. Explained variance was 0.54. In the inferior-temporal region, the arterial angle corresponding to the largest circle (P=0.002) was significant. Explained variance was 0.32.

Conclusions: The retinal blood vessel topography explains a significant part of the RNFB trajectory variability but only if (1) the vessel topography is assessed at an appropriate distance from the ONH and (2) the superior and inferior hemifield are addressed independently.

Introduction

Glaucoma is one of the important causes of blindness, with irreversible damage to retinal ganglion cells, the retinal nerve fiber layer (RNFL), and the optic nerve as its pathological features. The detection of changes in these structures is part of the diagnostic armamentarium in glaucoma; a detailed anatomical knowledge of especially the retinal nerve fiber bundle (RNFB) trajectories is helpful to integrate information from each structure and to topographically correlate it with visual field data.

In 2000, Garway-Heath et al.(2000) reported nerve fiber bundle trajectories based on fundus photographs. Later, models based on axonal growth and maps based on the correspondence between optical coherence tomography thickness measurements and visual field data were published (Airaksinen et al., 2008; Turpin et al., 2009; Ferreras et al., 2008; Kanamori et al., 2008). We developed a mathematical model describing the RNFB trajectories with their inter-subject variability, based on fundus photographs (Jansonius et al., 2009; Jansonius et al., 2012). A considerable variability was found, confirming the earlier findings (Garway-Heath et al., 2000). Recently, computational models mapping visual field locations to optic nerve head sectors were reported (Denniss et al., 2012; Carreras et al., 2014).

The influence of anatomical variables including refraction, axial length, optic disc position, and optic disc dimensions on the RNFB trajectories has been studied as well (Jansonius et al., 2012; Denniss et al., 2012; Lamparter et al., 2013). Although significant factors were identified, the sources of the variability of the RNFB trajectories are not fully understood.

It has been reported that the vascular and neuronal systems share many similarities. The blood vessels and nerves tend to develop in relative proximity, throughout the body of any species in general and in the primate retina in particular (Provis 2001; Carmeliet &Tessier-Lavigne 2005). In the primate

(human and macaque) retina, the vessels grow along the retinal ganglion cell layer/RNFL interface, except for the vessels in the vicinity of the fovea (Provis 2001). By using scanning laser polarimetry, Resch et al. (2011) reported that the peripapillary location of the main temporal superior and inferior blood vessels correlated with the RNFL thickness profile. In a recent study, Yamashita et al. reported that the retinal artery angle was highly correlated with the peak angle of the RNFL thickness (Yamashita et al., 2013). Given this close relationship between the retinal vasculature and the RNFL thickness profile in the peripapillary region, we hypothesize that the blood vessel pattern may be helpful to describe the RNFB trajectories.

The purpose of this study was to determine the relationship between the retinal vessel course and the variability of the RNFB trajectories as described by a mathematical model in the human retina.

Methods

Patient data and data acquisition

We used a previously collected dataset comprising 28 fundus pictures of the right eye of 28 subjects (Jansonius et al., 2012). These pictures were selected from patients who underwent digitized fundus photography as part of regular ophthalmic care in the University Eye Hospital Oulu, Finland. To ensure good visibility, only subjects without diseases affecting the RNFL or its visibility were included. As a consequence, most patients were relatively young (mean age 28 years) diabetic patients without diabetic retinopathy. Approval for the data collection was obtained according to the guidelines of the Ethical Committee of the Northern Ostrobothnia Hospital District. All subjects provided written informed consent. The study followed the tenets of the declaration of Helsinki.

Variability of the retinal nerve fiber bundle trajectories

Twenty-four trajectories per fundus photograph were traced, one per half clock-hour. Figure 1 shows an example of a traced photograph. The fitting process has been described before (Jansonius et al., 2009; Jansonius et al., 2012). In short, the trajectories were fitted in a modified polar coordinate system (r, φ), with r representing the distance from the center of the optic nerve head (ONH) and φ the corresponding angle. In this coordinate system, the trajectories were described by:

$$\phi(\phi_0, r) = \phi_0 + b(\phi_0)(r - r_0)^{c(\phi_0)} \quad (1)$$

where $\varphi_0 = \varphi(r=r_0)$ is the angular position of the trajectory at its starting point at a circle with radius r_0 around the center of the ONH, b a real number and c a positive real number. Parameter c determines the location of the curvature (punctum maximum of curvature close to the disc for $c < 1$ and further away from the disc for $c > 1$) while b determines the amount of curvature. The required nonlinear fitting was solved by performing a two-stage fitting process. In the first stage, the relationship between c and φ_0 was evaluated and substituted in Eq. (1). The second stage of the fitting process yielded an ln b (superior half of the retina) or ln(-b) (inferior half) value for each trajectory. The deviation of a trajectory from the previously published model was defined as the difference between the ln b or ln(-b) value of the trajectory and the corresponding ln b or ln(-b) value as predicted by the the model (Jansonius et al., 2009). The average difference within a region of interest was depicted by the variable 'mean departure (Jansonius et al., 2012). The mean departure was determined for each individual, for the superior-temporal (right eye clock hours 9 to 1) and the inferior-temporal (clock hours 5 to 9) region separately. The left column of Figure 2 shows, for the superior-temporal region, the original model (middle row) and the model +/- 1 standard deviation of mean departure (upper and lower row, respectively). The right column of Figure 2 presents the corresponding data for the inferior-temporal region. See legend to Fig. 2 for details. The standard deviation was 0.2 for both regions.

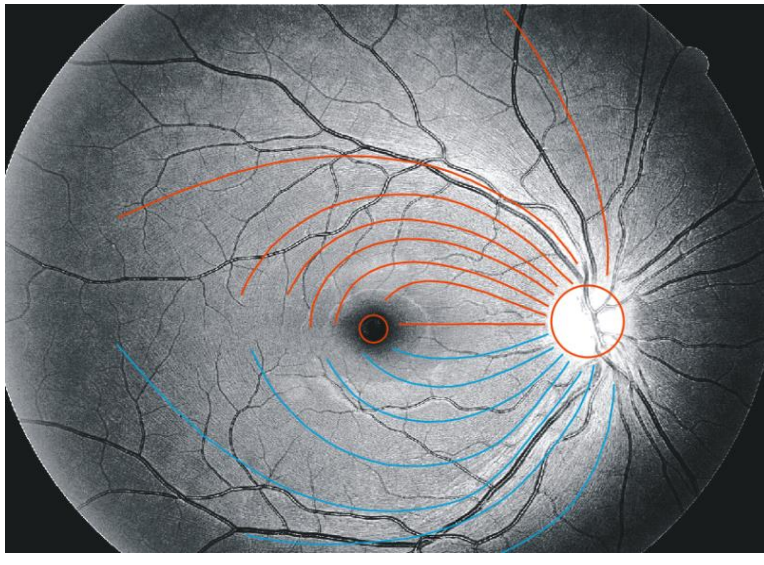

Figure 1. Example of a fundus photograph with traced trajectories. Colored areas depict the superior-temporal (red) and inferior-temporal (blue) region.

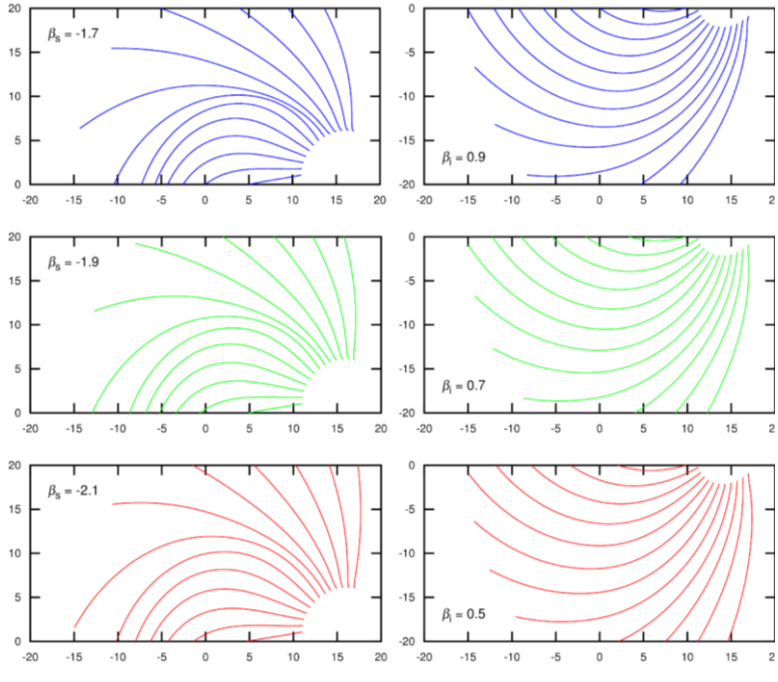

Figure 2. Original model (middle row) and model +/- 1 standard deviation of mean departure (upper and lower row, respectively) for the superior-temporal (left column) and inferior-temporal (right column) region. The *x* and *y* axis depict position (eccentricity) in degrees. Parameters β_s and β_i belong to the mathematical model (Jansonius et al., 2009); mean departure has to be added to the default values of these parameters (-1.9 for the superior-temporal region; 0.7 for the inferior-temporal region). See also the antepenultimate paragraph of the Discussion section.

Blood vessel angles

The Image J software (http://rsbweb.nih.gov/ij/; www.nih.gov, NIH, Bethesda, MD) was used in order to mathematically describe the retinal blood vessel courses. Firstly, a rectangle was fitted to the height and width of the ONH manually. Two diagonal lines were drawn and their crossing was considered as the ONH center. Three circles with radii equaling 25% (circle 1), 50% (circle 2), and 100% (circle 3) of the distance between the ONH center and the fovea were drawn around the ONH center. Figure 3 shows these circles. The intersections of the major temporal retinal blood vessels (superior artery, superior vein, inferior artery, and inferior vein) and the circles were determined. Subsequently, we measured the angles between a line through the ONH center and the fovea and the lines through the ONH center and the intersections. In this way, three series of four angles were defined: superior artery angle (SAAi), superior vein angle (SVAi), inferior artery angle (IAAi), and inferior vein angle (IVAi), where i is the circle number; Figure 3 shows the angles for i=2. Additionally, we marked the arteriovenous crossing of the first order away from the ONH in the superior-temporal and inferior-temporal region. In this way, another two angles were defined: superior crossing angle (SCA) and inferior crossing angle (ICA). These angles reflect the position of the vascular arcades and are also shown in Fig. 3. SAAi+IAAi and SVAi+IVAi correspond to the artery angle and vein angle as used by Yamashita et al. (2013), respectively. SCA+ICA corresponds to the "angle between temporal vessel arcades" as used by Flederius and Goldschmidt (2010).

Refraction and optic disc inclination

Refraction was recorded as the spherical equivalent refraction. The inclination of the ONH was quantified by the angle between a line through the ONH center and fovea and a horizontal line through the fovea.

Statistical analysis

The superior-temporal and inferior-temporal region were analyzed separately. The associations between mean departure on the one hand and blood vessel angles, refraction, and optic disc inclination on the other hand were analyzed with Pearson correlation analysis. Multiple linear regression analysis was used to determine the influence of refraction, optic disc inclination, and blood vessel angles on the mean departure. Initial multiple linear regression models were made for all three circles and for the crossing angle separately. Independent variables with $P>0.05$ were subsequently removed and the model with the highest adjusted R^2 - one model for each region - was considered the final model. All analyses were performed using R (version 2.11.1 for Linux; R Foundation for Statistical Computing, Vienna, Austria). For multiple linear regression, the lm function of R was used.

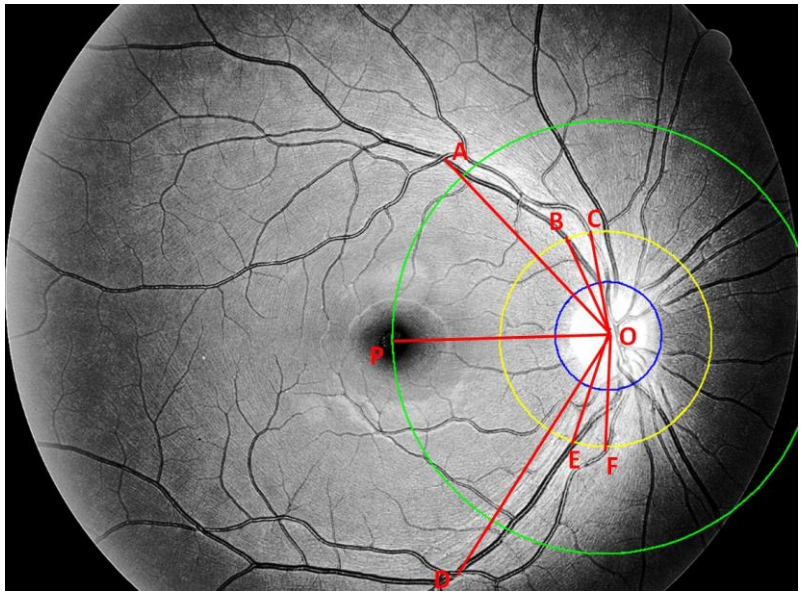

Figure 3. Blood vessel angles were defined at various distances from the optic nerve head (ONH) using the intersections of the major temporal retinal blood vessels (superior artery, superior vein, inferior artery, and inferior vein) and circles around the ONH center: superior arterial angle (SAA; C-P), superior venous angle (SVA; B-P), inferior arterial angle (IAA; F-P), and inferior venous angle (IVA; E-P). These angles were defined for circles with radii of 25% (circle 1; blue), 50% (circle 2; yellow; for this circle the angles are shown in the figure), and 100% (circle 3; green) of the ONH-fovea distance. Two more angles were defined using the arteriovenous crossing of the first order away from the ONH: superior crossing angle (SCA; A-P), and inferior crossing angle (ICA; D-P). Vertex at O for all angles.

Results

Table 1 shows the descriptive statistics of the involved variables. Table 2 presents the results of the corresponding correlation analysis. In the superior-temporal region, there was a significant association between mean departure and SAA1, SAA2, and refraction (i.e., spherical equivalent). In the inferior-temporal region, there was a significant association between mean departure and IAA3 and IVA2. Corresponding vessel angles from the superior and inferior hemifield were essentially not associated (all with P>0.07), nor were the mean departure superior-temporal and the mean departure inferior-temporal (r=0.21; P=0.27).

Tables 3 and 4 present the initial (Table 3) and final (Table 4) multiple linear regression models. The most significant (highest adjusted R^2) models were those involving circle 2 for the superior-temporal region and circle 3 for the inferior-temporal region. The overall explained variance (R^2) was 0.54 for the superior-temporal region and 0.32 for the inferior-temporal region. If only the vessel angles would be available, then the best model for the superior-temporal region is: Mean departure = 0.0132*SAA2 – 0.969.

Table 1. Characteristics of the included eyes (n=28)

	Median	IQR	Range
Mean departure superior-temporal	0.00	-0.11 to 0.18	-0.57 to 0.34
Mean departure inferior-temporal	0.09	-.075 to 0.21	-0.36 to 0.41
Refraction (D)	0.00	-1.25 to +1.13	-8.75 to +6.25
ONH inclination (deg)	4.8	3.7 to 6.9	0.8 to 10.6
SAA1 (deg)	86.8	79.9 to 93.4	59.9 to 109.5
SVA1(deg)	86.2	78.8 to 94.8	54.2 to 110.5
IAA1 (deg)	81.6	70.3 to 95.8	58.3 to 112.7
IVA1 (deg)	82.8	70.7 to 97.8	52.1 to 104.2
SAA2 (deg)	71.8	67.0 to 78.6	58.4 to 99.6
SVA2 (deg)	72.2	66.5 to 79.2	56.7 to 94.0
IAA2 (deg)	67.2	59.8 to 79.7	51.0 to 100.9
IVA2 (deg)	67.8	60.5 to 80.7	49.8 to 93.6
SAA3 (deg)	56.8	52.8 to 61.6	23.7 to 104.8
SVA3 (deg)	59.1	55.3 to 64.5	28.7 to 92.9
IAA3 (deg)	52.1	48.5 to 60.5	40.5 to 82.7
IVA3 (deg)	52.8	45.1 to 60.9	41.6 to 76.0
SCA (deg)	56.2	48.3 to 59.9	36.0 to 69.7
ICA (deg)	50.1	39.8 to 56.2	26.7 to 73.0

IQR = interquartile range; D = diopter; ONH = optic nerve head; SAAi (with i is 1, 2, or 3) = superior arterial angle measured at circle i (defined in Fig. 3); SVAi = superior venous angle measured at circle i; IAAi = inferior arterial angle measured at circle i; IVAi = inferior venous angle measured at circle i; SCA = superior crossing angle; ICA = inferior crossing angle.

Table 2. Correlation analysis between the mean departure (average individual deviation from the model) and refraction, ONH inclination, and the various blood vessel angles

	Mean departure superior-temporal		Mean departure inferior-temporal	
	r	P-value	r	P-value
Refraction	0.41	0.03	0.26	0.12
ONH inclination	-0.25	0.21	0.09	0.64
SAA1	0.44	0.02	/	/
SAA2	0.57	0.001	/	/
SAA3	0.24	0.22	/	/
SVA1	0.31	0.10	/	/
SVA2	0.28	0.15	/	/
SVA3	0.26	0.18	/	/
IAA1	/	/	0.26	0.19
IAA2	/	/	0.37	0.06
IAA3	/	/	0.57	0.002
IVA1	/	/	0.22	0.27
IVA2	/	/	0.41	0.03
IVA3	/	/	0.23	0.25
SCA	-0.12	0.56	/	/
ICA	/	/	0.27	0.17

ONH = optic nerve head; SAAi (with i is 1, 2, or 3)= superior arterial angle measured at circle i (defined in Fig. 3); SVAi = superior venous angle measured at circle i; IAAi = inferior arterial angle measured at circle i; IVAi = inferior venous angle measured at circle i; SCA = superior crossing angle; ICA = inferior crossing angle.

Table 3. R-squared, adjusted R-squared, and significant independent variables at P<0.05 of the initial multiple linear regression models as a function of the location at which the vessel angles were measured for the superior-temporal (A) and inferior-temporal (B) regions

	R^2	Adjusted R^2	Included independent variables (bold indicates significant at P<0.05)
A: superior-temporal			
Circle 1	0.42	0.32	Refr, **Inc**, **SAA1**, SVA1
Circle 2	0.54	0.46	**Refr**, **Inc**, **SAA2**, SVA2
Circle 3	0.33	0.22	**Refr**, Inc, SAA3, SVA3
Crossing	0.26	0.17	**Refr**, Inc, SCA
B: inferior-temporal			
Circle 1	0.16	0.01	Refr, Inc, IAA1, IVA1
Circle 2	0.35	0.24	Refr, Inc, **IAA2**, **IVA2**
Circle 3	0.39	0.28	Refr, Inc, **IAA3**, IVA3
Crossing	0.10	-.02	Refr, Inc, ICA

Refr = refraction; Inc = optic nerve head inclination; SAAi (with i is 1, 2, or 3) = superior arterial angle measured at circle i (defined in Fig. 3); SVAi = superior venous angle measured at circle i; IAAi = inferior arterial angle measured at circle i; IVAi = inferior venous angle measured at circle i; SCA = superior crossing angle; ICA = inferior crossing angle.

Table 4. Final multiple linear regression models for the superior-temporal (A) and inferior-temporal (B) region

	R^2	Adjusted R^2	Coefficient	Standard error	P-value
A: superior-temporal	0.54	0.49			
Intercept			-.748		
Refraction (D)			0.024	0.009	0.017
ONH inclination (deg)			-.031	0.012	0.021
SAA2 (deg)			0.012	0.003	<0.001
B: inferior-temporal	0.32	0.29			
Intercept			-.516		
IAA3			0.011	0.003	0.002

ONH = optic nerve head; SAA2 = superior arterial angle measured at circle 2 (defined in Fig. 3); IAA3 = inferior arterial angle measured at circle 3.

Discussion

In the superior-temporal region, refraction, ONH inclination, and SAA2 were the main determinants of the RNFB trajectories; in the inferior-temporal region IAA3 was the main determinant. Clearly, the site where the vessel topography is assessed is important: the optimal site was more close to the ONH superiorly (circle 2) than it was inferiorly (circle 3), and the location of the vascular arcades, as depicted by the crossing angle, did not provide any useful information. Arteries were more informative than veins.

In our earlier studies, we have demonstrated a significant inter-individual variability of the retinal nerve fiber bundle trajectories and addressed the role of refraction and ONH inclination (Jansonius et al., 2009; Jansonius et al., 2012). In the current study, both refraction and ONH inclination were significant in the

multivariable analysis, at least in the superior-temporal region (Table 4). This implies that refraction is associated with the RNFL trajectories. For ONH inclination, the significance could either reflect a truly independent effect or arise from the preprocessing of the fitting process (the ONH inclination influences the way a fundus picture is embedded in the modified polar coordinate system) (Jansonius et al., 2009). In both cases, adding information regarding ONH inclination to the model improves precision. For the current study it is important that the variability in ONH inclination is small compared to the variability in the vessel angles (Table 1). In the present study, the importance of the retinal blood vessel topography was uncovered. By adding information from the vessel topography, the explained variance increased from 0.28 and 0.08 (previous study) (Jansonius et al., 2012) to 0.54 and 0.32 (this study) for the superior-temporal and inferior-temporal region, respectively. As biological systems always show intrinsic variability, it is unlikely that much higher explained variances will be reached by adding more - currently unknown - determinants. Moreover, the tracing process itself also contributes to the variability (Denniss et al., 2014). For the dataset used in the current study, the inter-observer variability was addressed earlier (Jansonius et al., 2012). There was no bias between the two observers and the inter-observer variability was clearly smaller than the overall variability - albeit not negligible.

Our findings concerning the overall variability and the influence of refraction and ONH inclination on the RNFB trajectories agreed well with other studies (Garway-Heath et al., 2000; Denniss et al., 2012; Lamparter et al., 2013) and have been discussed in detail before (Jansonius et al., 2009; Jansonius et al., 2012). To the best of our knowledge, the significant influence of the retinal blood vessel topography on the RNFB trajectories has not been addressed before. However, an association between the retinal blood vessel positions and the peripapillary RNFL thickness profile has been reported, both with scanning laser polarimetry (at 3.2 mm from the ONH center) (Resch et al., 2011) and with optical coherence tomography (at 3.5 mm from the ONH center) (Yamashita et al., 2013; Pereira et al., 2014). In these studies, the effect of the blood vessels on the RNFL thickness

profile could have been, at least partially, an artifact due to a direct contribution of the blood vessels to the RNFL thickness profile measurement (Hood et al., 2008). This is not the case in our study, due to a different methodology (traced trajectories versus thickness measurements).

Why are the retinal blood vessel topography and the RNFB trajectories associated? Blood vessels and nerves tend to develop in relative proximity and the neuronal and vascular system may share common guidance signals during development (Provis 2001; Carmeliet & Tessier-Lavigne 2005; Dorrell & Friedlander 2006; Eichmann et al., 2005). The spindle cells, which become canalized later to form capillaries, invade the retina from the ONH and grow along the RGCL/RNFL interface (Provis 2001; Ashwell & Waite 2004). Because of the resulting close relationship between the neuronal and vascular system in the retina, one would expect to find a significant association between the retinal blood vessel topography and the RNFB trajectories all over the retina. However, the association seems to be limited to the vicinity of the ONH. In our study, the angles depicting the positions of the vascular arcades (SCA and ICA) were not associated with the RNFB trajectories. One possible explanation for this is the thick RNFL in the vicinity of the ONH, as opposed to the thin RNFL in areas that are further away from the ONH.

In the present study, the superior and inferior hemifield were studied separately. Both the RNFB trajectories and the vessel angles were essentially uncorrelated between the two hemifields (see Results section). Moreover, an RNFB trajectory asymmetry between the two hemifields was found previously (Jansonius et al., 2009; Jansonius et al., 2012). Joining the angles into artery angle (SAAi+IAAi) and vene angle (SVAi+IVAi) as described by Yamashita et al (2013) did not yield significant associations, nor did combining SCA and ICA as used by Flederius and Goldschmidt (results not shown) (Fledelius & Goldschmidt 2010). This indicates that the neuronal and vascular system share an asymmetry between the superior and inferior hemifields in the human retina.

A limitation of our study is the sample size - the sample comprised 28 eyes of 28 subjects. We addressed this, to some extent, by limiting the number of independent variables in our multivariable analysis. A larger Caucasian dataset and especially a repeat in other ethnicities should precede the use of our findings in health care applications.

How can our results be applied to build personalized models? For a given individual, mean departure values can be calculated for both hemifields using Table 4. Subsequently, a personalized model can be plotted using the previously published equations (Jansonius et al., 2009) with the calculated mean departure values added to ln *b* or ln(-*b*). This was illustrated in Fig. 2. This approach assumes that, for a given individual, the differences between the ln *b* or ln(-*b*) values of the traced trajectories and the corresponding values as predicted by the model are - within a region of interest - essentially independent of parameter φ_0 (the clock-hour) (Jansonius et al., 2009). Although this was not formally tested, it has to be the case because otherwise trajectories would cross in some regions and would leave other regions unwired. Neither of these situations is observed in reality.

The explained variances of 0.54 and 0.32 are not self-evident sufficiently high for an optimal assessment of glaucoma (Springelkamp et al., 2014). However, advances in optical coherence tomography (OCT) presumably allow for an individual measurement of the RNFB trajectories in the near future (Sugita et al., 2015). As the signal-to-noise ratio of such a measurement will be inherently limited, an underlying model that serves as a prior will always be needed as a starting point. Our model may serve as this starting point.

In conclusion, the retinal blood vessel topography explains a significant part of the distribution of the RNFL bundle trajectories in the human retina, but only if (1) the vessels are assessed at an appropriate distance from the ONH and (2) the superior and inferior hemifield are addressed independently. This should be taken

into account in future individualized mathematical models describing the RNFB trajectories.

References

Airaksinen PJ, Doro S, Veijola J. Conformal geometry of the retinal nerve fiber layer. Proc Natl Acad Sci U S A. 2008;105:19690-19695.

Ashwell KW and Waite P. Development of the peripheral nervous system. Paxinos G and Mai JK. The human nervous system, 2nd edition. Amsterdam, Elsevier Academic Press. 2004;95-110

Carmeliet P, Tessier-Lavigne M. Common mechanisms of nerve and blood vessel wiring. Nature 2005;436:193-200.

Carreras FJ, Medina J, Ruiz-Lozano M, Carreras I, Castro JL. Virtual tissue engineering and optic pathways: plotting the course of the axons in the retinal nerve fiber layer. Invest Ophthalmol Vis Sci. 2014;55:3107-3119.

Denniss J, McKendrick AM, Turpin A. An anatomically customizable computational model relating the visual field to the optic nerve head in individual eyes. Invest. Ophthalmol. Vis. Sci. 2012;53:6981-6990.

Denniss J, Turpin A, Tanabe F, Matsumoto C, McKendrick AM. Structure–function mapping: variability and conviction in tracing retinal nerve fiber bundles and comparison to a computational model. Invest Ophthalmol Vis Sci. 2014;55:728-736.

Dorrell MI, Friedlander M. Mechanisms of endothelial cell guidance and vascular patterning in the developing mouse retina. Prog Retin Eye Res. 2006;25:277-295.

Eichmann A, Makinen T, Alitalo K. Neural guidance molecules regulate vascular remodeling and vessel navigation. Genes Dev. 2005;19:1013-1021.

Ferreras A, Pablo LE, Garway-Heath DF, Fogagnolo P, García-Feijoo J. Mapping standard automated perimetry to the peripapillary retinal nerve fiber layer in glaucoma. Invest Ophthalmol Vis Sci. 2008;49:3018-3025.

Fledelius HC, Goldschmidt E. Optic disc appearance and retinal temporal vessel arcade geometry in high myopia, as based on follow-up data over 38 years. Acta Ophthalmol. 2010;88:514-520.

Garway-Heath DF, Poinoosawmy D, Fitzke FW, Hitchings RA. Mapping the visual field to the optic disc in normal tension glaucoma eyes. Ophthalmology. 2000;107:1809-1815.

Hood DC, Fortune B, Arthur SN, et al. Blood vessel contributions to retinal nerve fiber layer thickness profiles measured with optical coherence tomography. J Glaucoma. 2008;17:519-528.

Jansonius NM, Nevalainen J, Selig B et al. A mathematical description of nerve fiber bundle trajectories and their variability in the human retina. Vision Res. 2009;49:2157-2163.

Jansonius NM, Schiefer J, Nevalainen J, Paetzold J, Schiefer U. A mathematical model for describing the retinal nerve fiber bundle trajectories in the human eye: average course, variability, and influence of refraction, optic disc size and optic disc position. Exp Eye Res. 2012;105:70-78.

Kanamori A, Naka M, Nagai-Kusuhara A, Yamada Y, Nakamura M, Negi A. Regional relationship between retinal nerve fiber layer thickness and corresponding visual field sensitivity in glaucomatous eyes. Arch Ophthalmol. 2008;126:1500-1506.

Lamparter J, Russell RA, Zhu H, et al. The influence of intersubject variability in ocular anatomical variables on the mapping of retinal locations to the retinal nerve fiber layer and optic nerve head. Invest Ophthalmol Vis Sci. 2013;54:6074-6082.

Pereira I, Weber S, Holzer S, et al. Correlation between retinal vessel density profile and circumpapillary RNFL thickness measured with Fourier-domain optical coherence tomography. Br J Ophthalmol. 2014;98:538-543.

Provis JM. Development of the primate retinal vasculature. Prog Retin Eye Res. 2001;20:799-821.

Resch H, Brela B, Resch-Wolfslehner C, Vass C. Position of retinal blood vessels correlates with retinal nerve fibre layer thickness profiles as measured with GDx VCC and ECC. Br J Ophthalmol. 2011;95:680-684.

Springelkamp H, Lee K, Wolfs RCW, et al. Population-based evaluation of retinal nerve fiber layer, retinal ganglion cell layer, and inner plexiform layer as a diagnostic tool for glaucoma. Invest Ophthamol Vis Sci. 2014;55:8428-8438.

Sugita M, Pircher M, Zotter S, et al. Retinal nerve fiber bundle tracing and analysis in human eye by polarization sensitive OCT. Biomed Opt Express. 2015;6:1030-1054.

Turpin A, Sampson GP, McKendrick AM. Combining ganglion cell topology and data of patients with glaucoma to determine a structure-function map. Invest Ophthalmol Vis Sci. 2009;50:3249-3256.

Yamashita T, Asaoka R, Tanaka M, Kii Y, Yamashita T, Nakao K, Sakamoto T. Relationship between position of peak retinal nerve fiber layer thickness and retinal arteries on sectoral retinal nerve fiber layer thickness. Invest Ophthalmol Vis Sci. 2013;54:5481-5488.